Guo *et al. Biology Direct* (2024) 19:73
https://doi.org/10.1186/s13062-024-00514-w

Biology Direct

RESEARCH

Open Access

Reprogramming hematopoietic stem cell metabolism in lung cancer: glycolysis, oxidative phosphorylation, and the role of 2-DG

Ziqi Guo[1,2,3], Yaping Liu[1], Xin Li[1], Yuying Huang[1], Zuping Zhou[1,2*] and Cheng Yang[1,2,3*]

Abstract

Hematopoietic stem cells (HSCs) exhibit significant functional and metabolic alterations within the lung cancer microenvironment, contributing to tumor progression and immune evasion by increasing differentiation into myeloid-derived suppressor cells (MDSCs). Our aim is to analyze the metabolic transition of HSCs from glycolysis to oxidative phosphorylation (OXPHOS) in lung cancer and determine its effects on HSC functionality. Using a murine Lewis Lung Carcinoma lung cancer model, we conducted metabolic profiling of long-term and short-term HSCs, as well as multipotent progenitors, comparing their metabolic states in normal and cancer conditions. We measured glucose uptake using 2-[N-(7-Nitrobenz-2-oxa-1,3-diazol-4-yl)Amino]-2-Deoxyglucose (2-NBDG) and assessed levels of lactate, acetyl-coenzyme A, and ATP. Mitochondrial functionality was evaluated through flow cytometry, alongside the impact of the glucose metabolism inhibitor 2-DG on HSC differentiation and mitochondrial activity. HSCs under lung cancer conditions showed increased glucose uptake and lactate production, with an associated rise in OXPHOS activity, marking a metabolic shift. Treatment with 2-DG led to decreased T-HSCs and MDSCs and an increased red blood cell count, highlighting its potential to influence metabolic and differentiation pathways in HSCs. This study provides novel insights into the metabolic reprogramming of HSCs in lung cancer, emphasizing the critical shift from glycolysis to OXPHOS and its implications for the therapeutic targeting of cancer-related metabolic pathways.

Keywords Lung cancer, Hematopoietic stem cells, Metabolic reprogramming, Glycolysis, Oxidative phosphorylation, 2-DG, Tumor microenvironment

Introduction

Lung cancer stands as a primary cause of cancer-related deaths globally, posing persistent challenges to treatment strategies [1–3]. Despite advancements in understanding the pathophysiology of lung cancer that has fostered the development of novel treatment strategies, including immune checkpoint modulation and vaccine therapies, demonstrating improved overall survival rates in clinical trials compared to traditional treatment methods [4], the efficacy of treatments for lung cancer patients remains to be enhanced [5–7]. Within the tumor microenvironment, myeloid-derived suppressor cells (MDSCs) exert a potent inhibition on the anti-tumor immune response of cancer patients

*Correspondence:
Zuping Zhou
zhouzuping@mailbox.gxnu.edu.cn
Cheng Yang
yang_cheng1016@163.com
[1] School of Life Sciences, Guangxi Normal University, Guilin 541004, China
[2] Guangxi Universities Key Laboratory of Stem Cell and Biopharmaceutical Technology, Guangxi Normal University, Guilin 541004, China
[3] Key Laboratory of Ecology of Rare and Endangered Species and Environmental Protection, Guangxi Normal University, Guilin 541004, China

by suppressing the activity of $CD4^+$ T cells, $CD8^+$ T cells, and natural killer cells, thereby promoting tumor progression [8–12]. Consequently, immunotherapeutic strategies targeting MDSCs in lung cancer, such as promoting MDSCs differentiation, blocking their suppressive actions, or combining with chemotherapy and antibodies to eliminate these cells, are actively under research and development [13–16].

All immune cells, including MDSCs, originate from hematopoietic stem cells (HSCs) in the bone marrow, possessing the capacity for long-term self-renewal and differentiation into various mature immune cells [17–20]. Studies have revealed that HSCs might undergo aberrant activation in the tumor environment, leading to abnormal differentiation of downstream mature immune cells such as MDSCs, thereby fostering tumor development [18, 21–24]. Particularly, Wu et al. found alterations in the self-renewal, mobilization, and homing capacities of HSCs during tumorigenesis, notably increased numbers of granulocyte-monocyte progenitors (GMPs, precursors of MDSCs) in peripheral blood, closely linked to tumor progression and patient prognosis [22, 25–27].

In recent years, numerous studies have unveiled the close association between the metabolic reprogramming of HSCs and their proliferation, survival, and differentiation, with glucose metabolism levels particularly intertwined with the status of HSCs [28–30]. Aerobic glycolysis promotes the maintenance of dormant and quiescent state HSCs, while oxidative phosphorylation (OXPHOS) significantly increases with cell differentiation [31–33]. These findings suggest that by modulating the glucose metabolism of HSCs, the differentiation of immune cells could be influenced, providing novel insights for innovative tumor immunotherapeutic strategies based on metabolic interventions of HSCs [27, 34].

This study aims to explore the metabolic changes in HSCs in a mouse model of Lewis Lung Carcinoma (LLC) lung cancer and their impact on the tumor microenvironment. By investigating alterations in the glucose metabolism of HSCs in the context of LLC lung cancer, this study delves into how reshaping the glucose metabolism of HSCs influences the differentiation of cells, particularly the changes in the number of MDSCs in tumor-bearing mice. Our findings indicate significant alterations in glucose metabolism of HSCs within the LLC lung cancer mouse model, suggesting potential impacts on the types of immune cell differentiation, thus providing new insights and approaches for tumor treatment. Through these investigations, we seek to provide theoretical foundations and experimental guidance for modulating the differentiation and function of the immune system cells, paving the way for novel clinical applications.

Materials and methods

Experimental animals

In this study, we utilized female C57BL/6 J mice aged 2–3 months as experimental animals, which were provided by the Experimental Animal Resources Department of the Chinese Academy of Sciences. The experimental animals were housed and managed in the Key Laboratory of Stem Cell and Drug Biotechnology at Guangxi Normal University to ensure consistency and reproducibility of the experiments. All experimental procedures were approved by the Guangxi Normal University Ethics Committee for Experimental Animals (Approval No: GXNU-202103-017) in accordance with the "Guidelines for the Care and Use of Laboratory Animals" established by the Chinese Academy of Sciences. Moreover, throughout the experiment, we adhered to all relevant procedures according to the ARRIVE guidelines to ensure animal welfare. For humane euthanasia at the end of the experiments, we employed the widely recognized method of cervical dislocation to minimize the mice's suffering.

Purification of HSCs from mice using flow cytometry technology

In order to efficiently isolate and purify HSCs from mouse models, mice were euthanized around the inoculation site of LLC cells, and bone marrow samples were collected under sterile conditions. During sample collection, blood collection tubes containing anticoagulants were used to prevent blood clotting. Bone marrow cells were mixed thoroughly with an equal volume of physiological saline or PBS solution to prepare a mononuclear cell suspension. Subsequently, this suspension was mixed with a panel of specific fluorescently labeled antibodies (Lin-eFluor450, CD150-PerCP-eFluor710, Sca-1-PE-Cy7, CD48-APC, CD117-APC-eFluor780, all obtained from BD Biosciences) and incubated at 4 °C for 30 min to label the HSCs. Following labeling, the HSCs were precisely sorted and separated using a flow cytometer (FACS). The sorted HSCs were then collected in flow tubes containing 2 mL of complete DMEM culture medium for further experimental procedures.

Metabolic characteristics of HSCs in lung cancer by gas chromatography–mass spectrometry analysis

Initially, HSCs from lung cancer-bearing and normal control mice were accurately sorted using the FACS technique. The sorted cells were then washed twice with pre-chilled phosphate-buffered saline (PBS) to eliminate exogenous interference. Following washing, the cells underwent specific pretreatment procedures to disrupt the cell membrane and release intracellular metabolites. Subsequently, the released metabolites were qualitatively and quantitatively analyzed using gas chromatography-mass spectrometry

(GC–MS) technology. To explore the metabolic characteristics of HSCs and their alterations in the lung cancer environment, principal component analysis (PCA) was employed to determine overall differences between samples, while differential metabolite analysis was utilized to identify metabolic disparities between HSCs in tumor and normal states. Heat map analysis was employed to visually depict the expression patterns of key metabolites, and pathway analysis was performed to elucidate potential alterations in the metabolic pathways of HSCs under the influence of lung cancer.

Detection of cellular reactive oxygen species and mitochondrial membrane potential by FACS

To begin, single-cell suspension was obtained through trypsin treatment. Subsequently, cells were incubated in the dark with 10 mM dichlorodihydrofluorescein diacetate (DCFDA; provided by Invitrogen, USA) for 20 min at 37 °C to load the reactive oxygen probe. Following incubation, cells were washed with PBS three times for 5 min each to remove unbound DCFDA. Next, cells were incubated with surface antibodies for 30 min at 4 °C, with the entire process carried out in darkness to prevent photobleaching of the fluorescence. Upon antibody binding, 100 nM tetramethylrhodamine methyl ester (TMRM; provided by Immuno Chemistry Technologies, USA) was added, and thorough mixing by inversion ensured even distribution of TMRM to label the mitochondrial membrane potential. Finally, cells were centrifuged at 600 g for 4 min at 4 °C, the supernatant was discarded, and FACS technology was employed to assess mitochondrial membrane potential for the dual analysis of reactive oxygen species and membrane potential.

Mitochondrial reactive oxygen species (ROS) measurement

Mitochondrial ROS levels were assessed using mito-SOX red dye (M36008, Thermo Fisher, USA). Cells (2×10^4) were seeded on cover glasses placed in six-well plate inserts overnight. The following day, cells were treated with H_2O_2 (200 μM) for 24 h. Subsequently, cover glasses were washed with ice-cold 1×PBS and then incubated in a working solution of 2 μM mito-SOX at 37 °C for 30 min. After washing with 1×PBS, the cover glasses were mounted on slides. Images were captured using a multiphoton confocal microscope with a×100 objective lens and analyzed using the Nikon imaging software NIS Element [35].

Application of flow cytometry technology combined with immunofluorescence staining in the analysis of mitochondrial quality in HSCs

To analyze mitochondrial quality, we initially collected cells from mouse bone marrow and prepared them into single-cell suspensions. Subsequently, a series of pre-titrated antibodies including Lin-FITC (#22-7770-72, eBioscience, https://www.thermofisher.cn/cn/zh/antibody/product/Mouse-Hematopoietic-Lineage-Antibody-clone-17A2-RA3-6B2-M1-70-TER-119-RB6-8C5-Cocktail/22-7770-72), CD150-PerCP-eFluor710 (#46-1502-82, eBioscience, https://www.thermofisher.cn/cn/zh/antibody/product/CD150-Antibody-clone-mShad150-Monoclonal/46-1502-82), Sca-1-PE-Cy7 (#25-5981-82, eBioscience, https://www.thermofisher.cn/cn/zh/antibody/product/Ly-6A-E-Sca-1-Antibody-clone-D7-Monoclonal/25-5981-82), CD48-APC-eFluor780 (47-0481-82, eBioscience, https://www.thermofisher.cn/cn/zh/antibody/product/CD48-Antibody-clone-HM48-1-Monoclonal/47-0481-82), and CD117-PE-eFluor610 (#61-1171-82, eBioscience, https://www.thermofisher.cn/cn/zh/antibody/product/CD117-c-Kit-Antibody-clone-2B8-Monoclonal/61-1171-82) were added, followed by gentle mixing and incubation in the dark at 4 °C for 30 min. Next, Mito Tracker Deep Red (Cell Signaling, Shanghai, China; concentration 200 nM) or TOM20 (CL488-11802, 0.40 μg per 10^6 cells, Proteintech) were preheated to 37 °C and added to the cell suspension, which was then further incubated at 37 °C in the dark for 30 min to label the mitochondria. After labeling, FACS was employed for mitochondrial analysis. For immunofluorescence staining of mitochondrial quality, selected HSCs were seeded in 24-well plates at a density of 5×10^4 cells per well, and upon reaching 80% confluence, stained with preheated Mito Tracker Deep Red (concentration 500 nM) at 37 °C. Following staining, the cells were fixed with a methanol/acetic acid mixture (3:1) at −20 °C for 10 min, then incubated in the dark at 28 °C with DAPI solution (100 μL per well, concentration 15 μg/mL) for 15 min for nuclear staining. A fluorescence quenching agent was added, and the staining was observed and recorded under an inverted microscope. Additionally, the sorted HSCs were seeded in 96-well plates at a density of 1×10^4 cells per well, and after 24 h of in vitro culture, the culture supernatant was collected for lactate content analysis using a lactate assay kit (Abcam, UK) following the manufacturer's instructions.

Measurement of acetyl coenzyme A

In order to accurately measure the content of acetyl Coenzyme A in HSCs, precisely sorted HSCs were collected from experiments. Subsequently, the cell suspension was diluted to a concentration of 1×10^6 cells/mL using PBS. The cells were then lysed by repeated freeze–thaw cycles to release various cellular components. Following cell lysis, centrifugation at 1100×g for 20 min was performed to separate cell debris from the supernatant. After centrifugation, the supernatant was carefully collected to avoid disturbing the pellet. Finally, the

quantitative measurement of acetyl Coenzyme A content was conducted using the Acetyl Coenzyme A Assay Kit (provided by Abcam, product number #Cat No. ab87546, UK) following the manufacturer's instructions.

Measuring glucose uptake and intracellular ATP levels in HSCs

To assess the glucose uptake capacity and intracellular ATP levels of HSCs, precise sorting of HSCs from the experiment was essential. Following sorting, HSCs are seeded in 96-well plates, with a cell density of 1×10^4 cells per well. Prior to glucose uptake experiments, HSCs are pre-treated in a glucose-free culture medium to minimize background interference. Upon completion of pre-treatment, 50 nM of 2-[N-(7-Nitrobenz-2-oxa-1,3-diazol-4-yl)Amino]-2-Deoxyglucose (2-NBDG) (provided by Invitrogen, Cat. No. N13195) was added to each well and incubated at 37 °C for 30 min. During this process, 2-NBDG, a glucose analog, was used to evaluate the cells' glucose uptake capacity. After incubation, specific antibodies targeting surface markers of HSCs were added, and cellular uptake of 2-NBDG was quantitatively analyzed using FACS.

Intracellular ATP levels are measured using the ATP Determination Kit based on a luminescent ATP assay (provided by Sigma-Aldrich, Cat. No. D43223, USA) following the manufacturer's instructions. This assay kit allows for an accurate assessment of ATP levels within HSCs by reflecting ATP concentration through the intensity of fluorescence signals.

Metabolic measurements

The Seahorse XFe96 Extracellular Flux Analyzer (Agilent Technologies) was employed for metabolic analysis. Extracellular acidification rates (ECAR) and oxygen consumption rates (OCR) were calculated for each well. Cells were treated with injection compounds at the following concentrations for XF glycolysis stress test or XF Cell Mito test: 10 mM glucose (50-99-7, Sigma-Aldrich), 2 μM oligomycin (1404-19-9, Sigma-Aldrich), 50 mM 2-deoxy-D-glucose (2-DG) (154-17-6, Sigma-Aldrich), 1 μM carbonyl cyanide p-trifluoromethoxyphenylhydrazone (FCCP) (370-86-5, Sigma-Aldrich), and 0.5 μM rotenone (83-79-4, Sigma-Aldrich). The XF glycolysis stress test or XF Cell Mito test kits were procured from Agilent Technologies (USA) [36].

NADH determination

In order to quantify the levels of nicotinamide adenine dinucleotide (NADH) in HSCs, particularly to assess the accumulation of NADH during the process of mitochondrial OXPHOS, we sorted HSCs precisely into two groups. The first group of cells was treated with 2 mM antimycin A (AMA; provided by Sigma-Aldrich, product number Cat.No A8674, UK) at room temperature for 5 min. Antimycin A, a specific inhibitor of the mitochondrial electron transport chain, can block electron transfer within the mitochondria, resulting in reduced consumption of NADH and its accumulation within the cells. Following the treatment, the fluorescence intensity of NADH was detected through the UV440/40 nm channel using FACS. The second group of cells underwent no treatment and served as the control. By comparing the differences in NADH fluorescence before and after AMA treatment, the activity level of mitochondrial OXPHOS can be indirectly reflected. This method offers an effective means to assess mitochondrial function and cellular metabolic status.

Quantification of mitochondrial DNA copy number in HSCs using real-time quantitative PCR

To determine the copy number of mitochondrial DNA (mtDNA) in HSCs, the total DNA from HSCs needs to be extracted initially. This extraction was carried out using the DNA extraction kit provided by Tiangen (China) with the product code #Cat.NO DP304. Strict adherence to the kit's instructions during the experimental procedure was maintained to ensure the quality and efficiency of DNA extraction. The obtained total DNA comprises both mitochondrial and nuclear DNA.

Subsequently, real-time quantitative PCR (qPCR) was employed to quantitatively measure the copy number of mtDNA. In this step, the mitochondrial gene COXII (cytochrome C oxidase subunit II) was selected as the target to quantify the mtDNA copy number. Concurrently, β-Tubulin was chosen as the housekeeping gene for the nuclear genome to serve as an internal control and correct for variations in PCR reactions. The specific primer sequences for qPCR can be found in Table 1 accompanying the experiment.

CCK8

To assess the vitality of HSCs post-sorting, we employed the CCK8 (Cell Counting Kit-8) analysis method. Initially, post-sorted HSCs were seeded in a 96-well plate at a cell density of 2×10^3 cells per well. Subsequently, 10 μL

Table 1 qPCR Primer Sequences

Gene	Sequence (5′–3′)
COX2-F	TTCCAATCCATGTCAAAACCGT
COX2-R	AGTCCGGGTACAGTCACACTT
β-Tubulin-F	CAGGCCCGACAACTTTATCT
β-Tubulin-R	CTCTTTCCGCACGACATCTA

F forward, *R* reverse

of CCK8 solution (supplied by Beyotime, Cat No. C0037, China) was added to each well. This reagent reacts with enzymes in the cells to generate a measurable color change.

After a 4 h cell incubation, the 96-well plate was transferred to a constant temperature environment at 37 °C. The interaction of CCK8 with enzymes in viable cells produces a yellow-colored product, the absorbance of which can be detected at a wavelength of 450 nm using a spectrophotometer. The measured absorbance values are directly proportional to cell viability, where higher absorbance values indicate greater cellular vitality. This method was simple, rapid, and precise, allowing for the effective evaluation of HSC viability. T-HSCs were treated with 50 μM AZD3965 (ABS816101, Absin (Shanghai) Biotechnology Co., Ltd., https://www.absin.cn/azd3965/abs816101.html) for 24 h. The viability of T-HSCs was assessed [37].

Detection of apoptosis in HSCs

In order to accurately assess the apoptosis of HSCs, we utilized an apoptosis detection kit (provided by Beyotime, Cat No. C1062L, China). Initially, cultured cells were dissociated into single cells by trypsin digestion. Subsequently, the cells were gently resuspended in 195 μl of Annexin V-FITC binding buffer to ensure even distribution. Then, 5 μl of Annexin V-FITC was added to the suspension and gently mixed to bind to Phosphatidylserine (PS) of early apoptotic cells. Following this, 10 μl of propidium iodide (PI) staining solution was added and mixed gently again. Propidium iodide penetrates the compromised cell membrane of late-stage apoptotic or dead cells to bind with DNA.

Next, the cell mixture was incubated at room temperature (25 °C) in the dark for 10–20 min to allow sufficient time for Annexin V-FITC and PI to bind to the target cells. After the incubation, the samples were kept on ice and in the dark until flow cytometry analysis using a FACS was conducted. In the flow cytometer, green fluorescence emitted by Annexin V-FITC indicated early apoptotic cells, while red fluorescence from PI labeled late-stage apoptotic or already deceased cells.

LSK cells represent a distinct hematopoietic stem cell subset identified by the Lin- (negative) Sca-1^+ (positive) c-Kit^+ (positive) phenotype. The term "Lin" denotes the absence of lineage-specific surface markers such as CD3, CD4, CD8, B220, Gr-1, and Ter-119. Sca-1 and c-Kit serve as crucial markers for the identification and isolation of LSK cells.

Analysis of cell abundance in mouse bone marrow and spleen using flow cytometry

To analyze the abundance of various cell types in the bone marrow and spleen of mice, these tissues were first prepared into single-cell suspensions. The bone marrow cell suspension was then incubated with a series of specific surface antibodies, with Lin-FITC (#22-7770-72, eBioscience; https://www.thermofisher.cn/cn/zh/antibody/product/Mouse-Hematopoietic-Lineage-Antibody-clone-17A2-RA3-6B2-M1-70-TER-119-RB6-8C5-Cocktail/22-7770-72) labeling HSCs, Ter119-FITC marking erythroid cells (MA5-17821, eBioscience, https://www.thermofisher.cn/cn/zh/antibody/product/TER-119-Antibody-clone-TER119-Monoclonal/MA5-17821), Gr-1-APC (17-5931-82, eBioscience, https://www.thermofisher.cn/cn/zh/antibody/product/Ly-6G-Ly-6C-Antibody-clone-RB6-8C5-Monoclonal/17-5931-82), and CD11b-PE-Cy7 (557743, eBioscience, https://www.bdbiosciences.com/zh-cn/products/reagents/flow-cytometry-reagents/research-reagents/single-color-antibodies-ruo/pe-cy-7-mouse-anti-human-cd11b.557743) labeling myeloid cells, and CD3-APC (17-0032-82, eBioscience, https://www.thermofisher.cn/cn/zh/antibody/product/CD3-Antibody-clone-17A2-Monoclonal/17-0032-82), CD4-PE (12-0041-82, eBioscience, https://www.thermofisher.cn/cn/zh/antibody/product/CD4-Antibody-clone-GK1-5-Monoclonal/12-0041-82), CD8a-PE-Cy7 (25-0081-82, eBioscience, https://www.thermofisher.cn/cn/zh/antibody/product/CD8a-Antibody-clone-53-6-7-Monoclonal/25-0081-82), and B220-PerCP-Cy5.5 (45-0452-82, eBioscience, https://www.thermofisher.cn/cn/zh/antibody/product/CD45R-B220-Antibody-clone-RA3-6B2-Monoclonal/45-0452-82) marking lymphoid cells. Spleen cells were processed in a similar manner, using the same types of surface antibodies for labeling.

All cells were incubated at 4 °C, protected from light, for 30 min to allow the antibodies to fully bind to the cell surface antigens. Following incubation, FACS was performed for the detection and quantification of each cell type. This method effectively distinguishes different types of blood cells, such as red cells, white cell subsets, and HSCs, providing crucial information for studying cell dynamics and immune responses in animal models.

Statistical analysis

In this study, the collected data underwent statistical analysis and validation using the SPSS version 18.0 statistical software. Initially, a one-way analysis of variance (ANOVA) was conducted to compare differences among the various experimental groups. This step aimed to

examine whether a single factor at different levels significantly influenced the experimental data. Subsequently, a two-way ANOVA was employed to evaluate the impact of two independent variables and their interaction with the dependent variable. The two-way ANOVA facilitated the determination of whether the two distinct factors generated an interaction effect and how this effect influenced the experimental outcomes. The results were presented as mean ± standard deviation, with a p value < 0.05 indicating statistical significance and a p value < 0.01 denoting high statistical significance.

Results

Metabolic reprogramming and functional changes of HSCs in lung cancer: transition from glycolysis to OXPHOS

Metabolism plays a crucial role in maintaining the dormancy, activation, and differentiation of HSCs. In the process of lung cancer development, there is a significant increase in the number of HSCs, leading to upregulation of proliferation and differentiation towards more MDSCs compared to normal physiological conditions [38–40]. To investigate whether this metabolic shift regulates the function of HSCs, we performed metabolic profiling of HSCs in lung cancer. A mouse LLC lung cancer model was established, and after four weeks, we conducted metabolomic analysis on hematopoietic stem and progenitor cells (T-HSPCs) in the bone marrow, including long-term HSCs (LT-HSCs), short-term HSCs (ST-HSCs), and multipotent progenitors (MPPs) (Fig. 1A). The most significant changes in metabolites in comparison to the control group (N-HSPCs) were associated with glucose metabolism, such as levels of pyruvic acid, lactate, α-ketoglutarate, and glucose. Metabolic pathway enrichment analysis indicated a potential link between pyruvate metabolism and changes in HSPCs function (Fig. 1B–C).

Given the multiple fates of pyruvate, we analyzed the ratio of glycolysis to OXPHOS in HSCs. Long-term HSCs

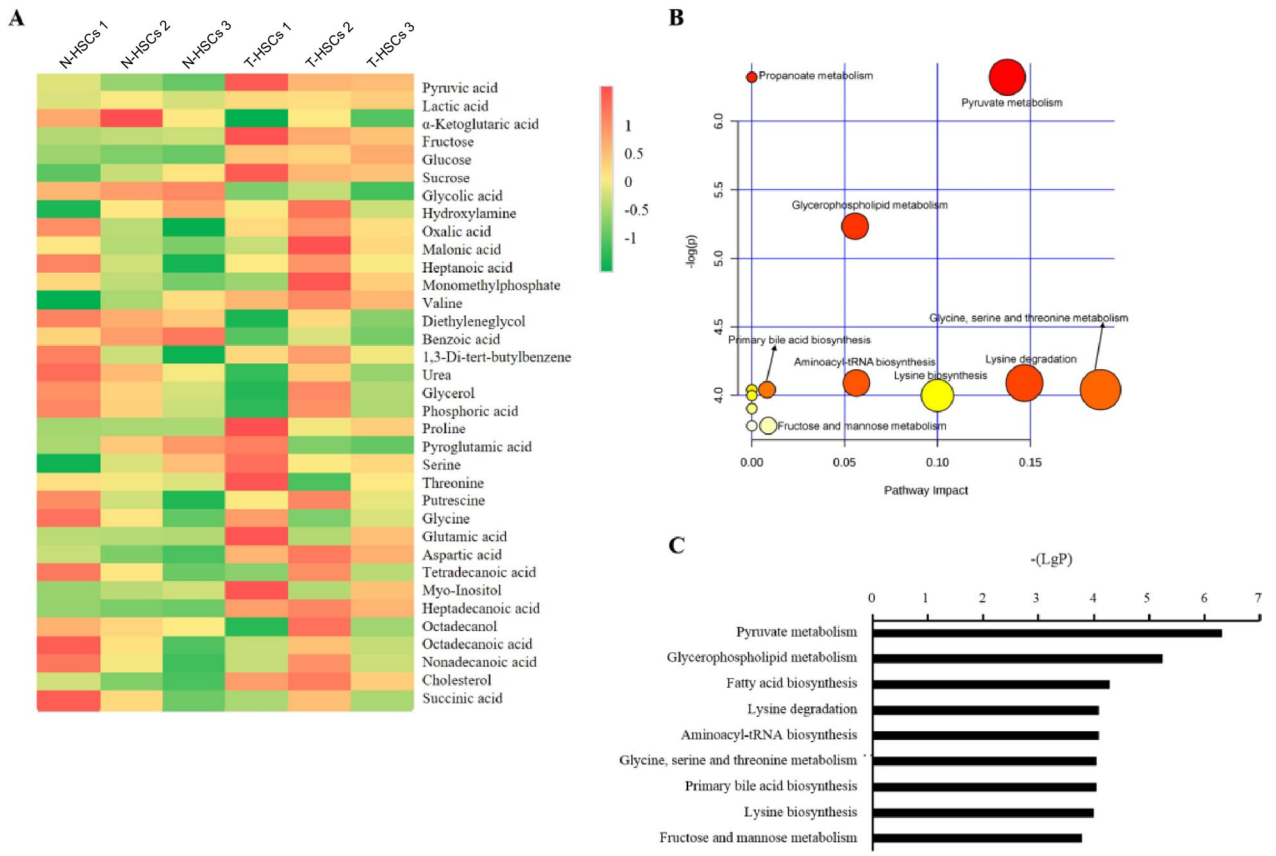

Fig. 1 Metabolic Analysis of LSK Cells in Lung Cancer. *Notes* **A** Comparison of the expression levels of different metabolites in LT-HSCs cells in normal and tumor states. The heat map shows the relative expression levels of various metabolites in N-HSCs and T-HSCs isolated from normal mouse bone marrow and tumor-bearing mouse bone marrow, respectively. **B** Enrichment analysis of metabolic pathways. The graph illustrates the correlation between different metabolic pathways and functional changes in LT-HSCs cells, with the height of the vertical axis indicating the degree of association between the pathway and the changes in LT-HSCs cell status. **C** Overview of significantly altered metabolites in comparison between N-HSCs and T-HSCs

isolated from normal and tumor-bearing mice (N-HSCs and T-HSCs, respectively) showed changes in glucose uptake in T-HSCs (Fig. 2A). Levels of lactate increased in T-HSCs (Fig. 2B), suggesting an upregulation of glycolysis. Additionally, substrates of OXPHOS, acetyl-CoA, and ATP levels were elevated in T-HSCs (Fig. 2C–D). LT-HSCs' oxygen consumption rate (OCR), indicative of oxidative phosphorylation (OXPHOS), and extracellular acidification rate (ECAR), reflective of aerobic glycolysis, were measured using the Seahorse device. The findings revealed a significant increase in both OCR and ECAR in T-HSCs, suggesting an upregulation of glycolysis (Fig. 2E–F). To confirm the changes in mitochondrial OXPHOS in T-HSCs, we introduced AMA, a specific inhibitor of the mitochondrial electron transport chain, to sorted HSCs and analyzed NADH levels after incubating the cells at 28 °C for 5 min. Accumulation of NADH in cells solely depends on mitochondrial OXPHOS in the presence of AMA. Post addition of AMA, an increase in NADH accumulation in T-HSCs indicated an upregulation of OXPHOS (Fig. 2G–H). The use of the monocarboxylate transporter protein MCT-1 inhibitor AZD3965 to treat T-HSCs resulted in a significant decrease in cell viability. This further demonstrates the reliance of HSCs on lactate production in lung cancer (Fig. 2I).

In conclusion, under the conditions of lung cancer, there are significant alterations in the glucose metabolism pathways of HSCs, particularly a transition from glycolysis to OXPHOS. This transition is reflected in the higher glucose uptake capacity, increased lactate levels, and upregulation of OXPHOS-related substrates in T-HSCs compared to N-HSCs. Especially under the action of antimycin A, T-HSCs exhibit enhanced OXPHOS activity, further confirming the metabolic shift in energy pathways of HSCs in the lung cancer microenvironment.

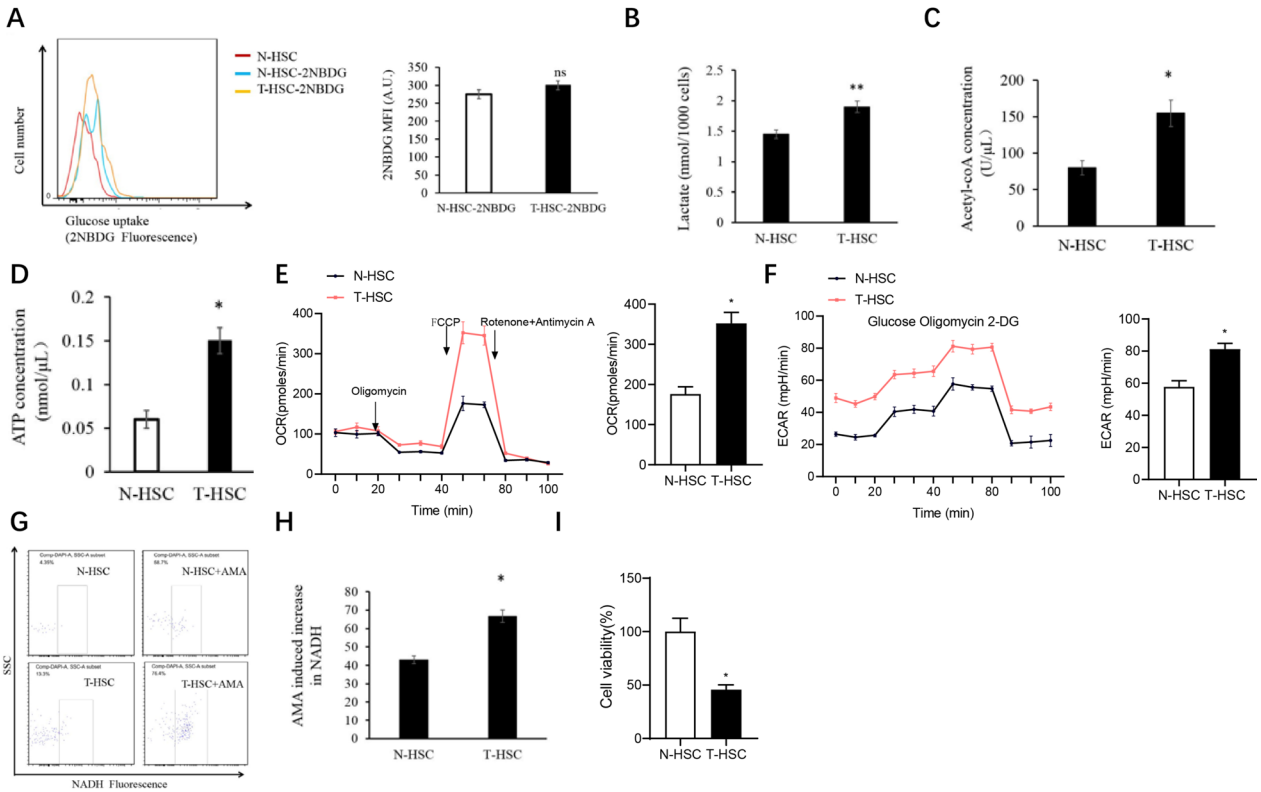

Fig. 2 Analysis of Glucose Metabolism in HSCs under Lung Cancer Conditions. *Note* **A** Comparison of glucose uptake between normal HSCs (N-HSCs) and lung cancer HSCs (T-HSCs) using 2-NBDG as a fluorescent probe (n = 3). **B** Measurement of lactate concentration showing a significant increase in lactic acid production per thousand cells in T-HSCs (n = 3; $^{**}p < 0.01$). **C** Determination of Acetyl-CoA concentration indicating potential enhancement of oxidative phosphorylation pathway in T-HSCs (n = 3; $^{*}p < 0.05$). **D** Assessment of ATP concentration revealing increased metabolic activity in T-HSCs (n = 3; $^{*}p < 0.05$). **E**–**F** The measurement of the oxygen consumption rate (OCR) and the extracellular acidification rate (ECAR) of LT-HSCs using the Seahorse equipment; **G** Cellular NADH representative spectra: Flow cytometry profiles before and after treatment with antimycin A (AMA) (n = 3); **H** Quantitative comparison of NADH accumulation induced by antimycin A; (I) Detection of the survival rate of T-HSCs using AZD3965 via CCK8 assay (n = 3; $^{*}p < 0.05$)

Enhanced oxidative phosphorylation and mitochondrial dynamics of HSCs in lung cancer

In the context of lung cancer, the mitochondrial metabolic activity of HSCs undergoes significant changes, particularly in OXPHOS, a process primarily occurring within the mitochondria, whose activation directly correlates with the enhancement of OXPHOS. In this study, we observed an increase in molecular markers related to OXPHOS in T-HSCs compared to normal-state HSCs (N-HSCs), indicating an upregulation of mitochondrial function in T-HSCs (Fig. 1). We performed quantitative analysis on mitochondria using FACS in combination with mitochondria-specific fluorescent dyes MitoTracker Deep Red and TOM20. Our findings revealed that the number of active mitochondria and total mitochondrial content in T-HSCs exceeded those in N-HSCs (Fig. 3A–D). Immunofluorescence analysis corroborated these results (Fig. 3E).

Furthermore, mitochondrial membrane potential (MMP) and reactive oxygen species (ROS) generation are crucial indicators for assessing mitochondrial functional status. Using tetramethylrhodamine ethyl ester (TMRE) as a fluorescent dye, we measured the MMP of HSCs and found that T-HSCs exhibited higher MMP levels ($p < 0.05$), accompanied by a significant increase in ROS production ($p < 0.01$), further supporting the notion of enhanced mitochondrial activity in T-HSCs (Fig. 4A–B). Furthermore, utilizing MitoSOX Red staining to detect mitochondrial reactive oxygen species (mROS) production, we observed elevated levels of mROS in T-HSCs (Fig. 4C). Real-time qPCR analysis also revealed a significant increase in mitochondrial DNA copy number in T-HSCs ($p < 0.01$), consistent with the observed elevation in mitochondrial quantity (Fig. 4D), indicating that under the influence of lung cancer, both the quantity and metabolic function of HSC mitochondria are enhanced.

Regulation of HSCs differentiation and mitochondrial activity in lung cancer through 2-DG-mediated glucose metabolism inhibition

Elevated glucose metabolism in T-HSCs leads to an increase in OXPHOS rate, suggesting that suppressing

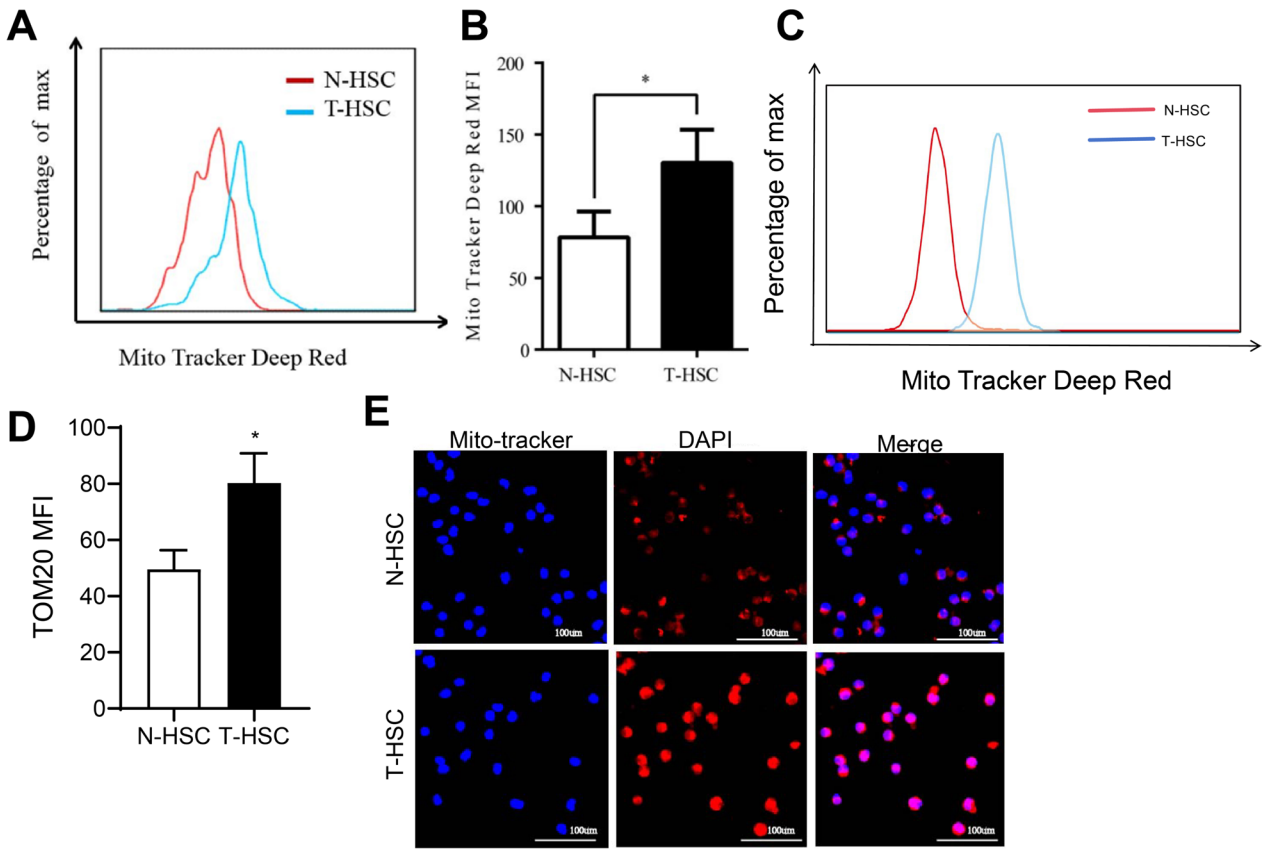

Fig. 3 Influence of Lung Cancer on Mitochondrial Mass of HSCs. *Note* **A** Representative images of N-HSCs and T-HSCs stained with MitoTracker Deep Red analyzed by flow cytometry. **B** Quantitative analysis of median fluorescence intensity (MFI) of MitoTracker Deep Red. **C** Representative images of TOM20 staining in N-HSCs and T-HSCs analyzed by flow cytometry. **D** Quantitative analysis of median fluorescence intensity (MFI) of TOM. **E** Immunocytochemical staining of mitochondrial dye MitoTracker Deep Red (red) and DAPI (blue) in N-HSCs and T-HSCs. (n = 5; *$p < 0.05$)

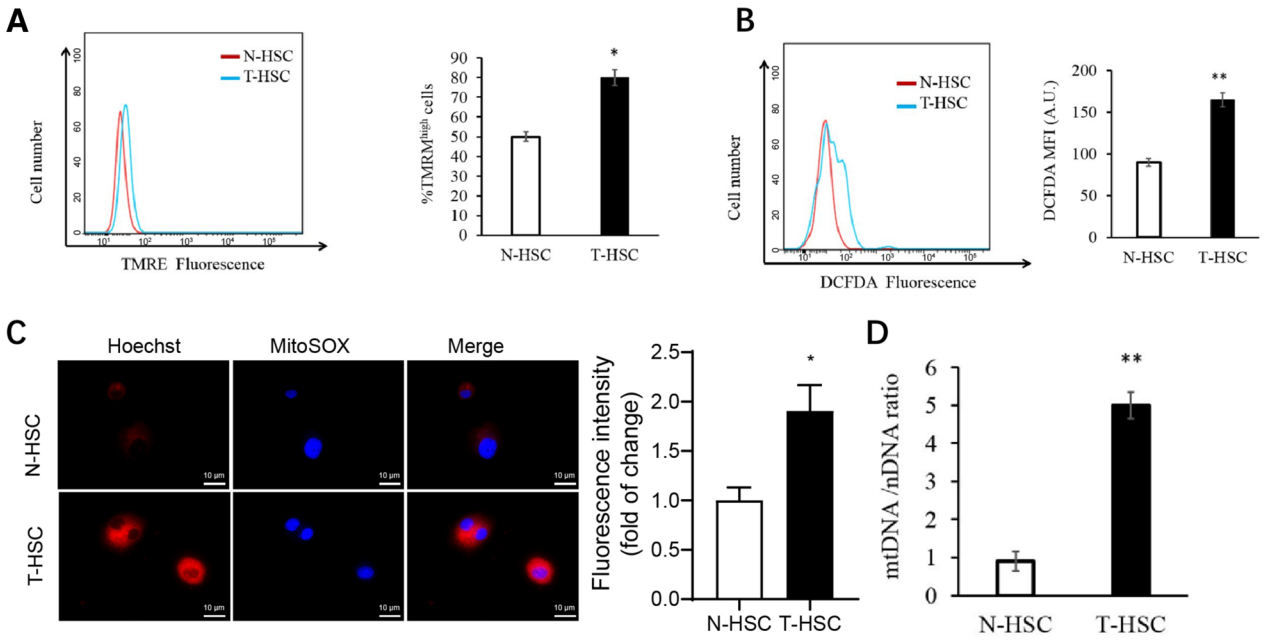

Fig. 4 Impact of Mitochondrial Activity on Conditioned HSCs in Lung Cancer. *Note* **A** (Left) Representative images from flow cytometry analysis of Tetramethylrhodamine Methyl Ester (TMRM) staining on N-HSC and T-HSC. (Right) Quantitative analysis of cells with high TMRM staining levels in N-HSC and T-HSC (n = 3; $*p < 0.05$). **B** (Left) Representative images from flow cytometry analysis of Dichlorodihydrofluorescein Diacetate (DCFDA) staining on N-HSC and T-HSC. (Right) Quantitative analysis of fold changes in DCFDA staining (n = 5; $**p < 0.01$). **C** Detection of mitochondrial reactive oxygen species (mROS) generation in N-HSCs and T-HSCs using MitoSOX Red staining. **D** Quantitative analysis of Mitochondrial DNA copy number relative to genomic DNA (n = 5; $**p < 0.01$)

glucose metabolism may impact their cellular functions. To investigate this, we injected glucose metabolism inhibitor 2-DG intravenously into mice and isolated HSCs from the bone marrow using flow cytometry one week later. Our results indicate that while 2-DG had minimal impact on the quantity of N-HSCs, it significantly reduced the proportion of T-HSCs (Fig. 5A). In vitro, cell viability assays revealed reduced proliferation (Fig. 5B) and decreased apoptosis of T-HSCs upon 2-DG treatment (Fig. 5C). These results indicate that the regulation of glucose metabolism by 2-deoxy-D-glucose (2-DG) can influence the state and function of hepatic stellate cells (HSCs), diminishing their activity. Under the presence of 2-DG, both the active mitochondria and total mitochondria count of activated hepatic stellate cells (T-HSCs) decrease, suggesting that 2-DG can reduce the numbers of active and total mitochondria in T-HSCs (Fig. 5D–G). Previous studies have identified specific subpopulations within HSCs that give rise to terminally differentiated cells [41–43]. By utilizing CD150, we distinguished HSCs subpopulations inclined towards lymphoid cell differentiation/steady state/myeloid cell differentiation (Ly-bi/Bala/My-bi HSCs), characterized as Lin-Sca-1$^+$c-Kit$^+$CD34$^-$CD135$^-$CD150$^-$, Lin-Sca-1$^+$c-Kit$^+$CD34$^-$CD135$^-$CD150^{low} and Lin-Sca-1$^+$c-Kit$^+$CD34$^-$CD135$^-$CD150$^+$ (Fig. 5H–I). Our results demonstrate a higher proportion of myeloid cell-differentiated subpopulations in T-HSCs compared to N-HSCs. During lung cancer progression, HSCs differentiate into myeloid cells. Interestingly, post 2-DG treatment, the proportion of HSCs subpopulations inclined towards myeloid cell differentiation decreased in T-HSCs, suggesting a potential inhibitory effect of 2-DG on the differentiation of HSCs into myeloid cells.

Metabolic intervention mediated by 2-dg modulates erythropoiesis and myeloid-derived suppressor cell differentiation dynamics in the bone marrow of lung cancer patients

Within the intricate microenvironment of lung cancer, the increase in bone marrow-derived MDSCs is closely associated with tumor immune evasion mechanisms, concomitant with alterations in red blood cells and specific T cell subpopulations. Subsequently, we investigated the impact of metabolic intervention mediated by 2-DG on the dynamics of bone marrow cells in a lung cancer mouse model, particularly on the regulation of red blood cells and MDSCs quantities, as well as the potential influence on the ratio of CD4$^+$ T cells and CD8$^+$ T cells.

The results indicate a significant increase in the number of red blood cells (Fig. 6A) and a notable decrease in MDSCs' quantity (Fig. 6B) in the bone marrow of lung

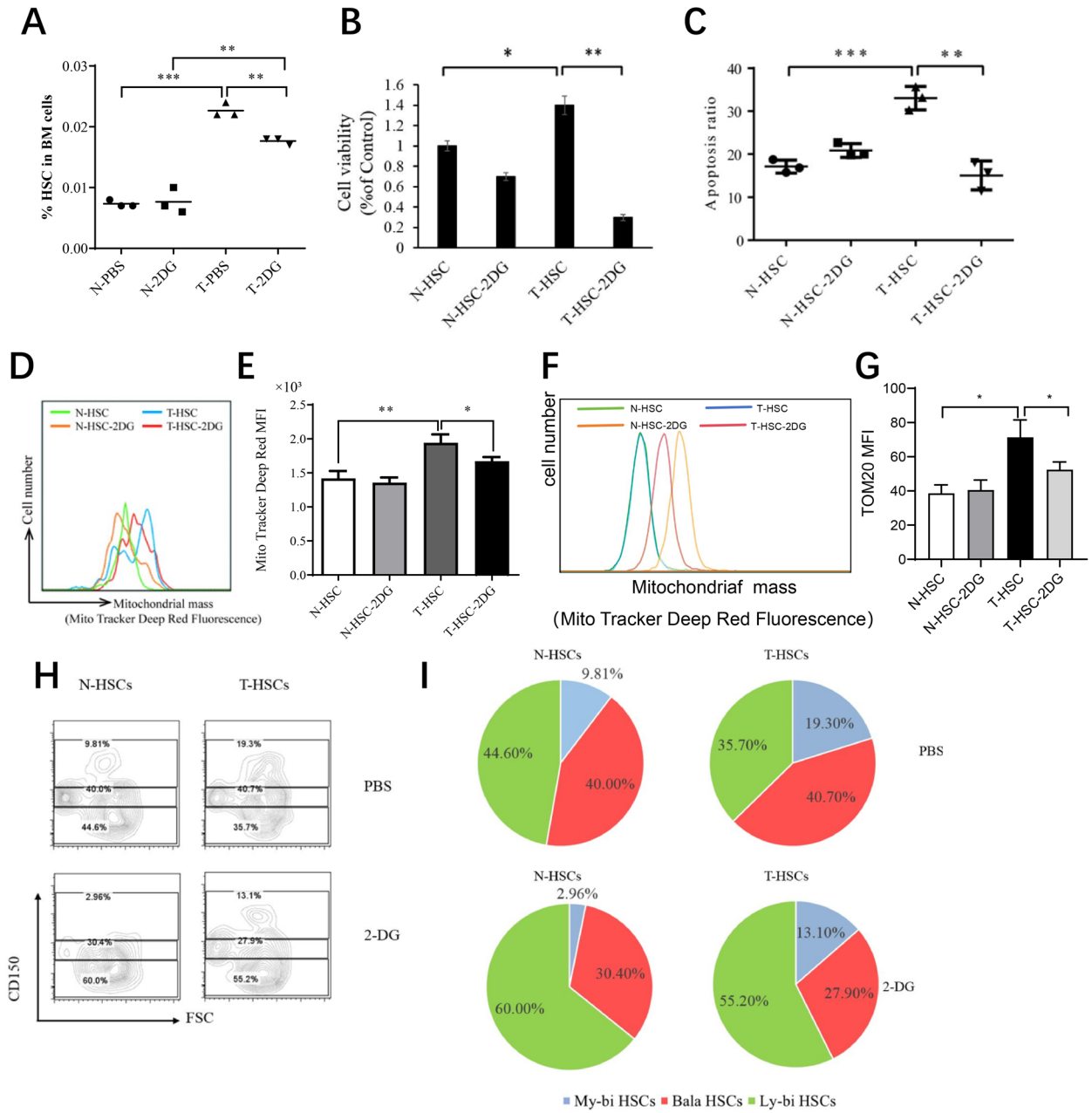

Fig. 5 Changes in T-HSC Function following 2-DG Stimulation. *Note* **A** Quantitative data of N-HSC and T-HSC percentages before and after 2-DG treatment (n = 3, *$p < 0.05$, **$p < 0.01$, ***$p < 0.001$). **B** CCK8 cell viability assay of N-HSC and T-HSC before and after 2-DG treatment (n = 3, *$p < 0.05$, **$p < 0.01$). **C** Analysis of apoptosis rates of N-HSC and T-HSC before and after 2-DG treatment (n = 3, *$p < 0.05$, **$p < 0.01$). **D** Representative images of Mito Tracker Deep Red staining of N-HSC and T-HSC before and after 2-DG treatment by flow cytometry. **E** Quantitative analysis of median fluorescence intensity (MFI) in Mito Tracker Deep Red assay (n = 3, *$p < 0.05$, **$p < 0.01$). **F** Flow cytometry analysis of representative images of TOM20 staining in N-HSCs and T-HSCs. **G** Quantitative analysis of median fluorescence intensity (MFI) of TOM. (H-I) Hematopoietic stem cell subtyping. Subtyping analysis of HSCs during tumorigenesis, as well as changes in hematopoietic stem cell subtypes before and after 2-DG stimulation. Myeloid biased HSCs (My-bi HSCs): $Lin^{-}Sca\text{-}1^{+}c\text{-}Kit^{+}CD34^{-}CD135^{-}CD150^{+}$; Balanced HSCs (Bala HSCs): $Lin^{-}Sca\text{-}1^{+}c\text{-}Kit^{+}CD34^{-}CD135^{-}CD150^{low}$; Lymphoid-biased HSCs (Ly-bi HSCs): $Lin^{-}Sca\text{-}1^{+}c\text{-}Kit^{+}CD34^{-}CD135^{-}CD150^{-}$

cancer mice post 2-DG treatment. This suggests that 2-DG, through metabolic pathways, modulates the lung cancer microenvironment by promoting erythropoiesis and inhibiting MDSC differentiation, potentially restoring a certain level of immune function. Noteworthy, the ratio of $CD4^{+}$ T cells and $CD8^{+}$ T cells showed no

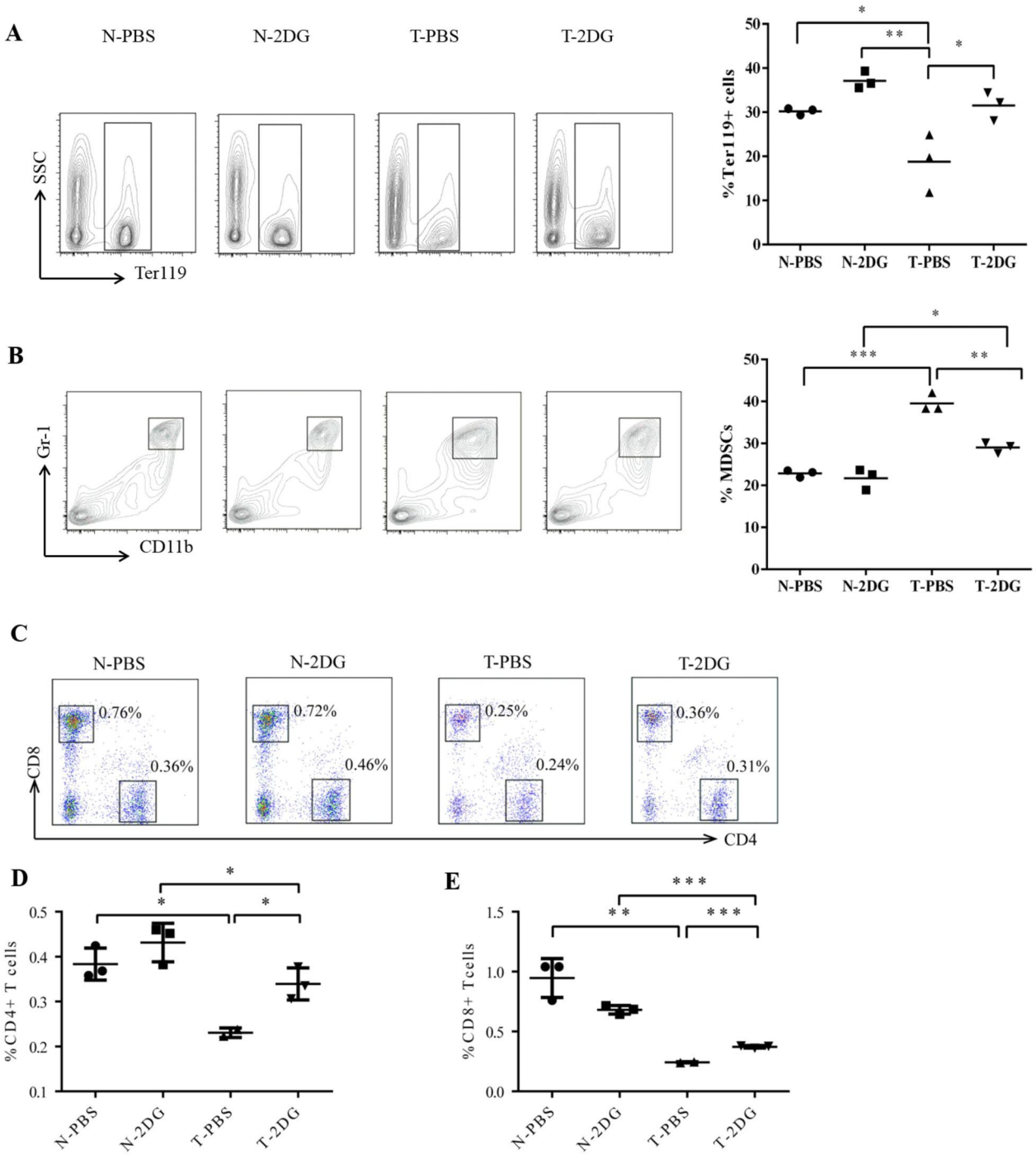

Fig. 6 Changes in the Bone Marrow Immune Cell Content after 2-DG Stimulation. *Note* **A** Representative image (left) of ter119$^+$ cell relative abundance in bone marrow before and after 2-DG treatment analyzed by flow cytometry. Quantitative data are presented on the right. **B** Representative image (left) of Gr1$^+$ CD11b$^+$ cell relative abundance in bone marrow before and after 2-DG treatment analyzed by flow cytometry. Quantitative data are presented on the right. **C** Representative image (up) of CD4$^+$ and CD8$^+$ T cell relative abundance in bone marrow before and after 2-DG treatment analyzed by flow cytometry. **D** Quantitative data for CD4$^+$ T cell proportion before and after 2-DG treatment in bone marrow are depicted. **E** Quantitative data for CD8$^+$ T cell proportion before and after 2-DG treatment in bone marrow are provided as well. All experiments were conducted thrice. ***$p < 0.001$, **$p < 0.01$, *$p < 0.05$

significant changes after 2-DG treatment (Fig. 6C–E), implying that the metabolic intervention mediated by 2-DG predominantly affects specific cell populations rather than broadly impacting all immune cell types.

In conclusion, this study unveils the significant effects of metabolic intervention mediated by 2-DG on erythropoiesis and MDSC differentiation dynamics in the bone marrow microenvironment of lung cancer, laying an experimental groundwork for further exploration of metabolic-targeting strategies in lung cancer therapy.

Effect of 2-DG on splenic myeloid-derived suppressor cell proportion and its role in red blood cell homeostasis in lung cancer mice

2-DG, as a well-known inhibitor of sugar metabolism, merits particular attention for its impact on the immune cell population [44]. The research findings indicate that the impact of 2-deoxy-D-glucose (2-DG) treatment on spleen size is relatively limited (Fig. 7A), suggesting a minimal direct effect on spleen structure. However, 2-DG demonstrates significant effects in regulating specific immune cell populations within the spleen. Specifically, 2-DG treatment significantly increases the proportion of red blood cells (Fig. 7B) and decreases the proportion of MDSCs (Fig. 7C–D). These results are consistent with the effects observed in the bone marrow environment, indicating that 2-DG can exert similar immunomodulatory effects in different immune organs through specific metabolic pathways.

Furthermore, the impact of 2-DG on the proportion of $CD4^+$ T cells, $CD8^+$ T cells, and B cells in the spleen is not significant (Fig. 7E–H), underscoring the selective action of 2-DG in modulating specific immune cell subsets, particularly MDSCs. These findings suggest that the metabolic intervention mechanism of 2-DG may be associated with its ability to inhibit specific stem cell differentiation into myeloid lineage cells, although this hypothesis requires further validation through additional research.

In summary, 2-DG effectively reduces the proportion of MDSCs in the spleen of lung cancer mice through metabolic intervention, with minimal impact on maintaining red blood cell homeostasis.

Gene expression analysis reveals the molecular characteristics and metabolic regulation of HSCs under tumorigenic conditions

To further elucidate the impact of T-HSCs, we compared the gene expression patterns of T-HSCs and N-HSCs. The expression heatmap revealed 199 differentially expressed genes between these two cellular subtypes, comprising 44 upregulated genes such as *Rcvrn*, *Vldlr*, *Gpr65*, and *Car5b*, as well as 155 downregulated genes including *Ccl6*, *Jchain*, *Mpo*, *Prss34*, and *Mcpt8* (Fig. 8A). These genes are implicated in cell cycle regulation, RNA degradation, and ribosome biogenesis (Fig. 8B–C). Figure 8D enumerates the most significantly altered genes. Microarray findings were validated through real-time qPCR (Fig. 8E), providing concrete evidence supporting our microarray analysis. Additionally, we examined the expression of genes related to glucose metabolism such as, *Ldhd*, *Pdk2*, *Lkb1*, and *Sirt7*. The results were consistent with previous data, suggesting that genes associated with glycolysis and oxidative phosphorylation may be upregulated.

Discussion

In our in-depth investigation of the metabolic changes of LT-HSCs in lung cancer and their impact on the tumor microenvironment, our research has revealed a series of remarkable biological phenomena and potential therapeutic targets, offering a fresh perspective and strategies for lung cancer treatment. Our findings not only align with existing literature [31, 45] but also push the boundaries of knowledge in this field. Particularly, we have for the first time unveiled the shift in metabolic preferences of LT-HSCs under lung cancer conditions and how this shift influences cell differentiation and the tumor microenvironment, presenting novel targets for cancer therapy.

Previous research has shown that LT-HSCs primarily rely on glycolysis rather than OXPHOS for energy production under static conditions. However, the proportion of OXPHOS increases gradually as the cells differentiate [31,

(See figure on next page.)

Fig. 7 Changes in Splenic Immune Cell Content After 2-DG Stimulation. *Notes* **A** Effects of 2-DG treatment on spleen size (right) and body weight (left) in mice. **B** Representative flow cytometry analysis of the relative abundance of $Ter119^+$ cells in the spleen before and after 2-DG treatment (left). Quantitative data are presented on the right. **C** Representative flow cytometry analysis of the relative abundance of $CD11b^+$ cells in the bone marrow before and after 2-DG treatment (left). Quantitative data are presented on the right. **D** Representative flow cytometry analysis of the relative abundance of $Gr1^+$ cells in the bone marrow before and after 2-DG treatment (left). Quantitative data are presented on the right. **E** Representative flow cytometry analysis of the relative abundance of $CD4^+$ T cells and $CD8^+$ T cells in the bone marrow before and after 2-DG treatment. (F) Quantitative data on the proportion of $CD4^+$ T cells in the spleen before and after 2-DG treatment. (G) Quantitative data on the percentage of $CD8^+$ T cells in the spleen before and after 2-DG treatment. (H) Quantitative data on the percentage of $B220^+$ cells in the spleen before and after 2-DG treatment. (n = 3; $^{***}p < 0.001$, $^{**}p < 0.01$, $^{*}p < 0.05$)

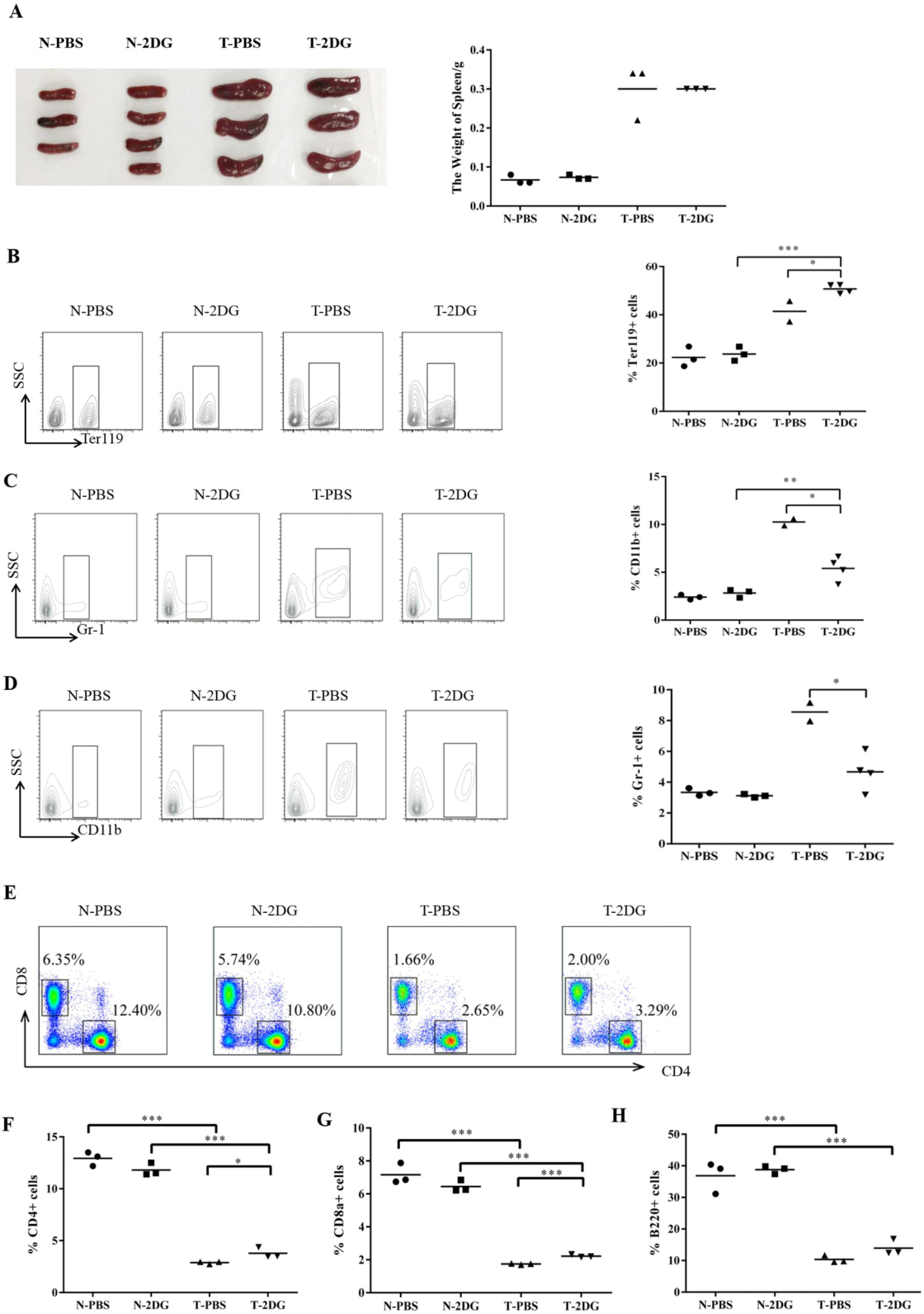

Fig. 7 (See legend on previous page.)

45]. Our study has revealed a significant metabolic shift, which is evident not only in the energy metabolism pattern shifting from glycolysis-dependent to more OXPHOS utilization but also in the adjustment of metabolic balance. This transition unveils the adaptive response of LT-HSCs to the lung cancer microenvironment, aiming to efficiently meet their energy and biosynthetic demands, further deepening our understanding of the metabolic adaptability of stem cells in the tumor microenvironment.

Furthermore, we have observed that metabolic reprogramming under lung cancer conditions not only affects the energy metabolism pattern of HSCs but also significantly influences their differentiation fate [46]. Specifically, tumor-induced metabolic changes promote the differentiation tendency of HSCs towards PMN-MDSCs, a process that may exacerbate tumor progression and adverse outcomes [26, 47–49]. Whether the differentiation bias of HSCs is related to metabolic reprogramming remains unclear. Our research indicates that a metabolic shift occurs in LT-HSCs during tumorigenesis, transitioning from a reliance on glycolysis to a combination of OXPHOS and glycolytic metabolism. The impact of aberrant glucose metabolism induced by tumorigenesis on the differentiation of LT-HSCs has also been confirmed. Inhibiting glucose metabolism can reverse the imbalance in LT-HSC differentiation, leading to reduced MDSC production. Metabolomic analysis of purified HSPCs suggests changes in their metabolism under tumor conditions, with a significant increase in acetate metabolism (Fig. 1). Levels of acetate and lactate increase in T-HSPCs, indicating that glycolytic metabolism in T-HSCs has not diminished. However, acetyl-CoA and NADH levels increase, mitochondrial mass and DNA copy numbers rise, and ROS and ATP levels are upregulated (Figs. 2, 3), indicating an increase in the rate of OXPHOS in T-HSCs. While glycolysis and OXPHOS are known to be interconnected [50, 51], our results demonstrate an increase in both glycolysis and OXPHOS in T-HSCs. Immunofluorescence results (Fig. 3) show a similar number of cells marked by MitoTracker Red in N-HSCs and T-HSCs. However, the mitochondrial mass is notably increased in T-HSCs, indicating a metabolic shift from glycolysis to OXPHOS in a subset of cells. OXPHOS can generate over 18 times more ATP than glycolysis, and T-HSCs exhibit limited ATP production capacity, confirming that only a fraction of cells undergo metabolic transformation [52]. Cells undergoing metabolic transition in T-HSCs may also undergo functional changes that lead to differentiation imbalance.

By intervening in the metabolism of HSCs in lung cancer patients with metabolic inhibitors like 2-DG, we have demonstrated that altering the metabolic state can regulate the differentiation preference of HSCs and reduce the potential for MDSC production [43, 53–55]. This strategy may not only enhance the immune response in lung cancer patients but also help suppress tumor progression and metastasis by modifying the tumor microenvironment [56, 57].

While our research has made significant progress in understanding the metabolic changes of HSCs in lung cancer and their impact on the tumor microenvironment, many questions remain unanswered, such as how tumor-induced metabolic reprogramming regulates the differentiation fate of HSCs at the molecular level and how to precisely utilize metabolic intervention strategies to optimize lung cancer treatment [58]. Future research will need to delve deeper into these mechanisms and validate the clinical application potential of metabolic interventions [59].

In conclusion, our study provides a new understanding of the metabolic reprogramming of HSCs under lung cancer conditions and its impact on cell differentiation and the tumor microenvironment, offering new mechanistic insights into tumor progression and laying a scientific foundation for the development of novel treatment strategies based on metabolic interventions. These findings underscore the importance of further investigating the metabolic adaptability of HSCs in the tumor microenvironment and their significance as therapeutic targets.

Conclusion

This study reveals a significant metabolic reprogramming of HSCs during tumor development, particularly in the context of lung cancer. Specifically, T-HSCs no longer rely solely on glycolysis but also depend on OXPHOS. This metabolic shift is accompanied by an increased differentiation tendency of HSCs toward MDSCs, thus promoting tumor progression and metastasis. Moreover, treatment with 2-DG alters the metabolic profile of T-HSCs, leading to a significant reduction in the number of MDSCs, potentially aiding in inhibiting tumor growth (Fig. 9).

(See figure on next page.)

Fig. 8 Identification of Differentially Expressed Genes in N-HSCs and T-HSCs. *Note* **A** Heat map showing the gene expression changes in N-HSCs and T-HSCs (n = 3). **B** Functional analysis of differentially expressed genes using Gene Ontology (GO). **C** Pathway analysis of differentially expressed genes using Kyoto Encyclopedia of Genes and Genomes (KEGG). **D** Top 20 differentially expressed genes in T-HSCs. (E) qPCR validation of genes related to glycolysis and OXPHOS

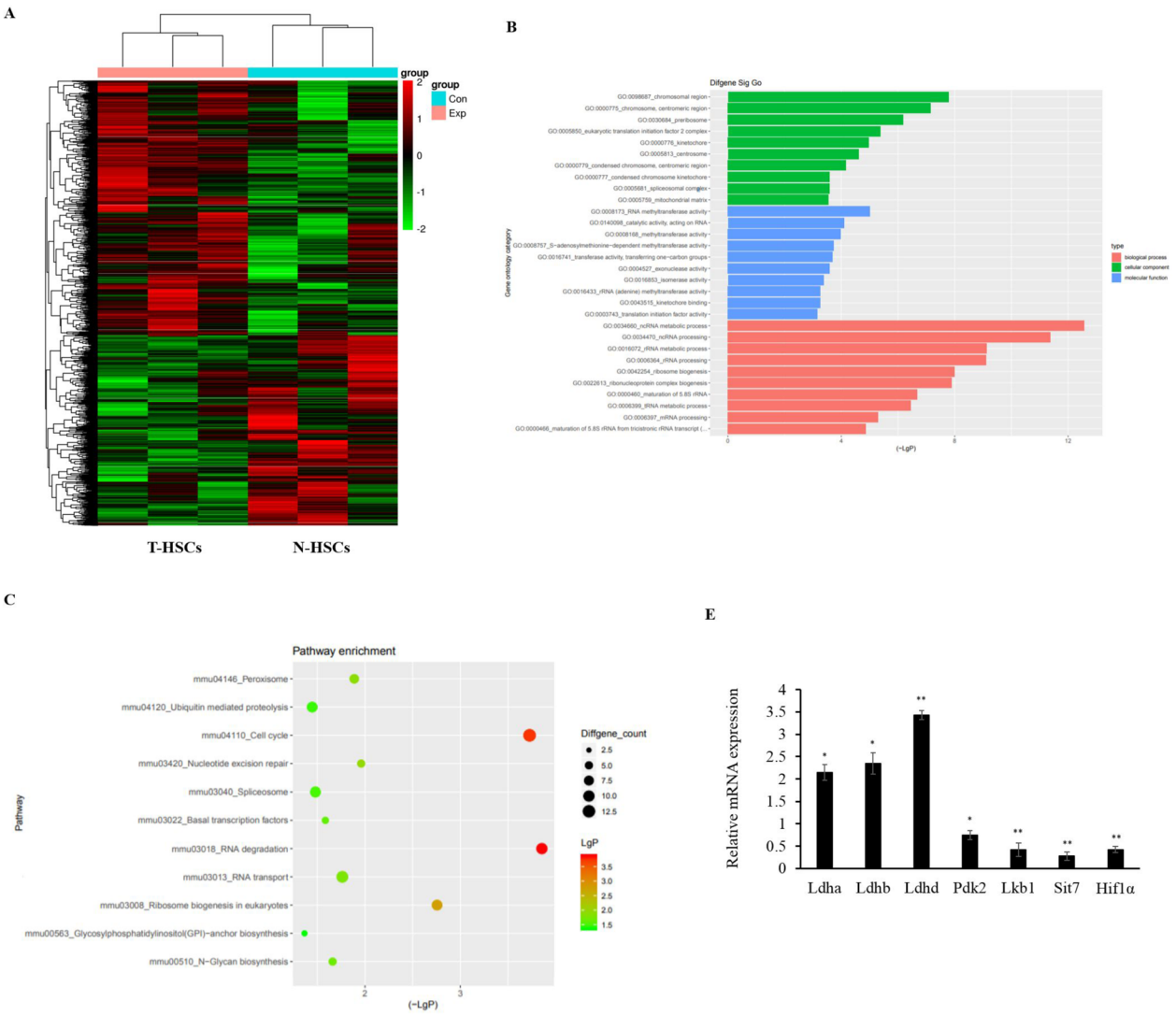

D

Gene_Accession	symbol	Gene_Description	Fold	diffState
NM_009038	Rcvrn	recoverin	5.27	up
NM_001161420	Vldlr	very low density lipoprotein receptor	4.12	up
XM_011239917	Gm21994	predicted gene 21994	3.39	up
NM_008152	Gpr65	G-protein coupled receptor 65	3.18	up
NM_181315	Car5b	carbonic anhydrase 5b, mitochondrial	2.85	up
NM_021396	Pdcd1lg2	programmed cell death 1 ligand 2	2.49	up
NM_009899	Clca3a1	chloride channel accessory 3A1	2.59	up
NM_011347	Selp	selectin, platelet	2.58	up
NM_013748	Clnk	cytokine-dependent hematopoietic cell linker	2.48	up
NM_183264	Tespa1	thymocyte expressed, positive selection associated 1	2.50	up
NM_181596	Retnlg	resistin like gamma	0.21	down
NM_013599	Mmp9	matrix metallopeptidase 9	0.20	down
NM_007895	Ear2	eosinophil-associated, ribonuclease A family, member 2	0.20	down
NM_001310438	Ly6g	lymphocyte antigen 6 complex, locus G	0.18	down
XM_001477102	I830127L07Rik	RIKEN cDNA I830127L07 gene	0.18	down
NM_001173460	Sirpb1b	signal-regulatory protein beta 1B	0.18	down
NM_009139	Ccl6	chemokine (C-C motif) ligand 6	0.18	down
NM_152839	Jchain	immunoglobulin joining chain	0.17	down
NM_010824	Mpo	myeloperoxidase	0.15	down
NM_178372	Prss34	protease, serine 34	0.11	down
NM_008572	Mcpt8	mast cell protease 8	0.07	down

Fig. 8 (See legend on previous page.)

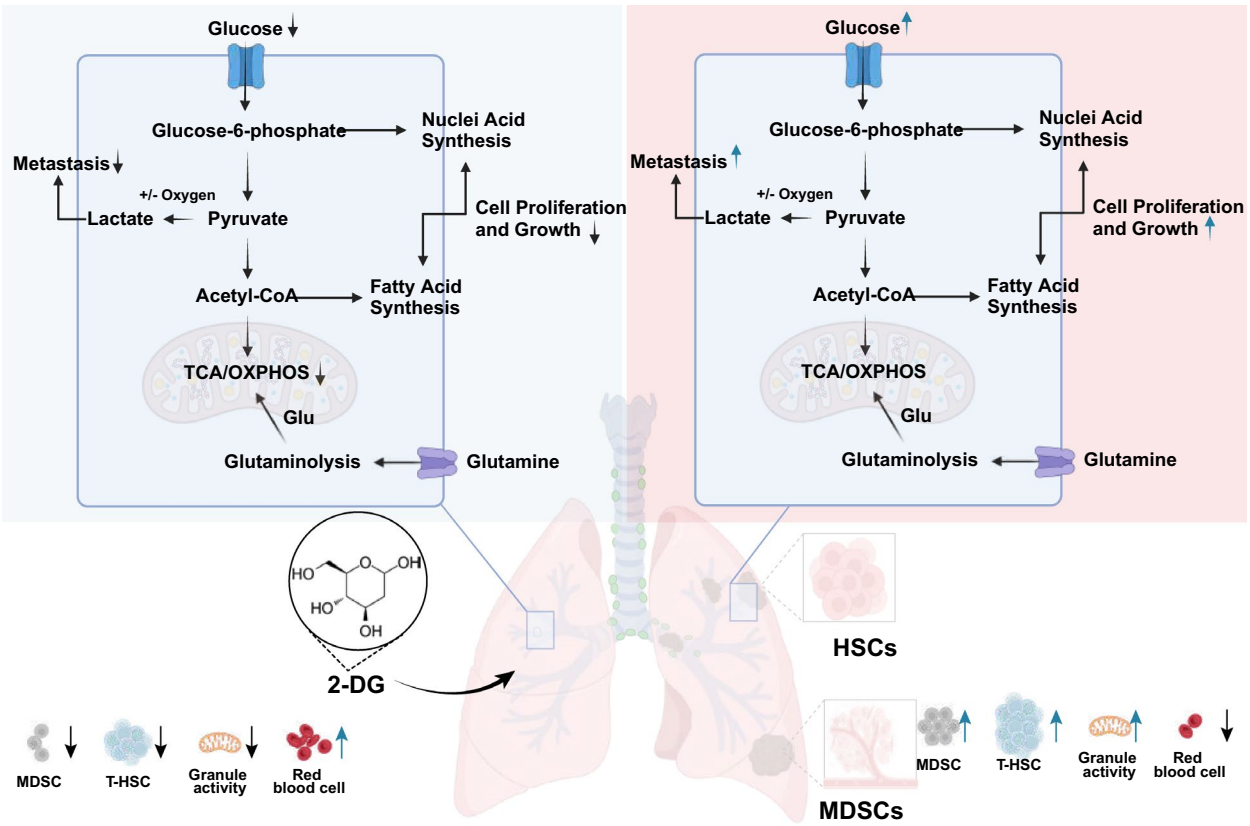

Fig. 9 Graphical Summary of Metabolic Reprogramming of HSCs in Lung Cancer: Impact of 2-DG-Mediated Glycolysis Inhibition on the Immune Microenvironment

Continuing the exploration of this study, these findings are not only scientifically significant, particularly in understanding the impact of the tumor microenvironment on immune cell function, but also hold great value for clinical applications. In the field of lung cancer therapy, this research provides a theoretical basis for novel therapeutic approaches targeting HSCs' metabolic pathways. These new strategies may help alleviate the tumor-promoting immunosuppressive environment, offering new hope for lung cancer patients.

However, the limitations of this study lie in its reliance on mouse models, potentially differing from the tumor environment in humans. Additionally, the research primarily focuses on the metabolic changes in HSCs without addressing other tumor types or the effects on other immune cell types. The long-term effects of 2-DG treatment and its potential impacts on normal tissues are areas of future research that need attention. Looking ahead, further validation of these findings in human cells or more complex in vivo models, and exploration of the effects of different tumor types on immune cell metabolism, are desired. The clinical prospects of 2-DG and other metabolic interventions, including their safety, efficacy, and effects on normal cells, require in-depth investigation. These efforts will contribute to a deeper understanding of the metabolic mechanisms in the tumor microenvironment and offer new strategies for the treatment of lung cancer and other tumors.

Abbreviations

HSCs	Hematopoietic stem cells
MDSCs	Myeloid-derived suppressor cells
FACs	Flow cytometry sorting
HE	Hematoxylin–eosin staining

Acknowledgements
Thanks to Yaping Liu and Xin Li for providing experimental technical support.

Author contributions
Ziqi Guo: Conceptualization, Methodology, Investigation, Writing—Original Draft, Visualization. Yaping Liu: Data Curation, Formal Analysis, Writing—Review & Editing. Xin Li: Methodology, Validation, Resources. Yuying Huang: Investigation, Resources, Data Curation. Zuping Zhou: Supervision, Project Administration, Funding Acquisition, Writing—Review & Editing. Cheng Yang: Conceptualization, Supervision, Project Administration, Funding Acquisition, Writing—Review & Editing.

Funding
This study was supported by National Natural Science Foundation of China (32160159), National Science Foundation of Guangxi (2022GXNSFBA035546), National Natural Science Foundation of China (81972700, 32260188) and Key R&D projects in Guangxi (GuikeAB22080071).

Availability of data and materials
No datasets were generated or analysed during the current study.

Declarations

Ethical approval
All experimental procedures were approved by the Guangxi Normal University Ethics Committee for Experimental Animals (Approval No: GXNU-202103-017), in accordance with the "Guidelines for the Care and Use of Laboratory Animals" established by the Chinese Academy of Sciences.

Consent for publication
Not applicable.

Competing interest
The authors declare no competing interests.

Received: 15 April 2024 Accepted: 8 August 2024
Published: 24 August 2024

References

1. Siegel RL, Miller KD, Jemal A. Cancer statistics. CA Cancer J Clin. 2015;65(1):5–29. https://doi.org/10.3322/caac.21254.
2. Sun R, Hou Z, Zhang Y, Jiang B. Drug resistance mechanisms and progress in the treatment of EGFR-mutated lung adenocarcinoma. Oncol Lett. 2022;24(5):408. https://doi.org/10.3892/ol.2022.13528.
3. Sedeta E, Sung H, Laversanne M, Bray F, Jemal A. Recent mortality patterns and time trends for the major cancers in 47 countries worldwide. Cancer Epidemiol Biomarkers Prev. 2023;32(7):894–905. https://doi.org/10.1158/1055-9965.EPI-22-1133.
4. Hall RD, Gray JE, Chiappori AA. Beyond the standard of care: a review of novel immunotherapy trials for the treatment of lung cancer. Cancer Control. 2013;20(1):22–31. https://doi.org/10.1177/107327481302000105.
5. Crosby D, Bhatia S, Brindle KM, et al. Early detection of cancer. Science. 2022;375(6586):eaay9040. https://doi.org/10.1126/science.aay9040.
6. Frankell AM, Dietzen M, Al Bakir M, et al. The evolution of lung cancer and impact of subclonal selection in TRACERx. Nature. 2023;616(7957):525–33. https://doi.org/10.1038/s41586-023-05783-5.
7. Arroyo-Hernández M, Maldonado F, Lozano-Ruiz F, Muñoz-Montaño W, Nuñez-Baez M, Arrieta O. Radiation-induced lung injury: current evidence. BMC Pulm Med. 2021;21(1):9. https://doi.org/10.1186/s12890-020-01376-4.
8. Gabrilovich DI, Nagaraj S. Myeloid-derived suppressor cells as regulators of the immune system. Nat Rev Immunol. 2009;9(3):162–74. https://doi.org/10.1038/nri2506.
9. Ma J, Xu H, Wang S. Immunosuppressive role of myeloid-derived suppressor cells and therapeutic targeting in lung cancer. J Immunol Res. 2018;2018:6319649. https://doi.org/10.1155/2018/6319649.
10. Pai JA, Hellmann MD, Sauter JL, et al. Lineage tracing reveals clonal progenitors and long-term persistence of tumor-specific T cells during immune checkpoint blockade. Cancer Cell. 2023;41(4):776-790.e7. https://doi.org/10.1016/j.ccell.2023.03.009.
11. Huang M, Xiong D, Pan J, et al. Targeting glutamine metabolism to enhance immunoprevention of EGFR-driven lung cancer. Adv Sci (Weinh). 2022;9(26): e2105885. https://doi.org/10.1002/advs.202105885.
12. Briere DM, Li S, Calinisan A, et al. The $KRAS^{G12C}$ inhibitor MRTX849 reconditions the tumor immune microenvironment and sensitizes tumors to checkpoint inhibitor therapy. Mol Cancer Ther. 2021;20(6):975–85. https://doi.org/10.1158/1535-7163.MCT-20-0462.
13. Wang Y, Tian J, Wang S. The potential therapeutic role of myeloid-derived suppressor cells in autoimmune arthritis. Semin Arthritis Rheum. 2016;45(4):490–5. https://doi.org/10.1016/j.semarthrit.2015.07.003.
14. Dong S, Guo X, Han F, He Z, Wang Y. Emerging role of natural products in cancer immunotherapy. Acta Pharm Sin B. 2022;12(3):1163–85. https://doi.org/10.1016/j.apsb.2021.08.020.
15. Ravi A, Hellmann MD, Arniella MB, et al. Genomic and transcriptomic analysis of checkpoint blockade response in advanced non-small cell lung cancer. Nat Genet. 2023;55(5):807–19. https://doi.org/10.1038/s41588-023-01355-5.
16. Sheida F, Razi S, Keshavarz-Fathi M, Rezaei N. The role of myeloid-derived suppressor cells in lung cancer and targeted immunotherapies. Expert Rev Anticancer Ther. 2022;22(1):65–81. https://doi.org/10.1080/14737140.2022.2011224.
17. Kikuchi I, Inoue S, Sakaguchi E, Ono T. Regressing nevoid nail melanosis in childhood. Dermatology. 1993;186(2):88–93. https://doi.org/10.1159/000247314.
18. Long H, Jia Q, Wang L, et al. Tumor-induced erythroid precursor-differentiated myeloid cells mediate immunosuppression and curtail anti-PD-1/PD-L1 treatment efficacy. Cancer Cell. 2022;40(6):674-693.e7. https://doi.org/10.1016/j.ccell.2022.04.018.
19. Matsushima K, Yang D, Oppenheim JJ. Interleukin-8: an evolving chemokine. Cytokine. 2022;153: 155828. https://doi.org/10.1016/j.cyto.2022.155828.
20. Kouroukli O, Symeonidis A, Foukas P, Maragkou MK, Kourea EP. Bone marrow immune microenvironment in myelodysplastic syndromes. Cancers (Basel). 2022;14(22):5656. https://doi.org/10.3390/cancers14225656.
21. Long NA, Golla U, Sharma A, Claxton DF. Acute myeloid leukemia stem cells: origin, characteristics, and clinical implications. Stem Cell Rev Rep. 2022;18(4):1211–26. https://doi.org/10.1007/s12015-021-10308-6.
22. Sahin E, Depinho RA. Linking functional decline of telomeres, mitochondria and stem cells during ageing. Nature. 2010;464(7288):520–8. https://doi.org/10.1038/nature08982.
23. Yu S, Ren X, Li L. Myeloid-derived suppressor cells in hematologic malignancies: two sides of the same coin. Exp Hematol Oncol. 2022;11(1):43. https://doi.org/10.1186/s40164-022-00296-9.
24. Ramachandra N, Gupta M, Schwartz L, et al. Role of IL8 in myeloid malignancies. Leuk Lymphoma. 2023;64(11):1742–51. https://doi.org/10.1080/10428194.2023.2232492.
25. Kleppe M, Spitzer MH, Li S, et al. Jak1 integrates cytokine sensing to regulate hematopoietic stem cell function and stress hematopoiesis. Cell Stem Cell. 2018;22(2):277. https://doi.org/10.1016/j.stem.2017.12.018.
26. Wu WC, Sun HW, Chen HT, et al. Circulating hematopoietic stem and progenitor cells are myeloid-biased in cancer patients. Proc Natl Acad Sci USA. 2014;111(11):4221–6. https://doi.org/10.1073/pnas.1320753111.
27. Vainchenker W, Yahmi N, Havelange V, Marty C, Plo I, Constantinescu SN. Recent advances in therapies for primary myelofibrosis. Fac Rev. 2023;12:23. https://doi.org/10.12703/r/12-23.
28. García-Prat L, Sousa-Victor P, Muñoz-Cánoves P. Proteostatic and metabolic control of stemness. Cell Stem Cell. 2017;20(5):593–608. https://doi.org/10.1016/j.stem.2017.04.011.
29. Liu L, Patnana PK, Xie X, et al. GFI1B acts as a metabolic regulator in hematopoiesis and acute myeloid leukemia. Leukemia. 2022;36(9):2196–207. https://doi.org/10.1038/s41375-022-01635-9.
30. Mobet Y, Liu X, Liu T, Yu J, Yi P. Interplay between m^6A RNA methylation and regulation of metabolism in cancer. Front Cell Dev Biol. 2022;10:813581. https://doi.org/10.3389/fcell.2022.813581.
31. Papa L, Djedaini M, Hoffman R. Mitochondrial role in stemness and differentiation of hematopoietic stem cells. Stem Cells Int. 2019;2019:4067162. https://doi.org/10.1155/2019/4067162.
32. Qing Y, Dong L, Gao L, et al. R-2-hydroxyglutarate attenuates aerobic glycolysis in leukemia by targeting the FTO/m^6A/PFKP/LDHB axis. Mol Cell. 2021;81(5):922-939.e9. https://doi.org/10.1016/j.molcel.2020.12.026.
33. Yan JS, Yang MY, Zhang XH, et al. Mitochondrial oxidative phosphorylation is dispensable for survival of $CD34^+$ chronic myeloid leukemia stem and progenitor cells. Cell Death Dis. 2022;13(4):384. https://doi.org/10.1038/s41419-022-04842-5.
34. Mitroulis I, Ruppova K, Wang B, et al. Modulation of myelopoiesis progenitors is an integral component of trained immunity. Cell. 2018;172(1–2):147-161.e12. https://doi.org/10.1016/j.cell.2017.11.034.
35. Tai P, Chen X, Jia G, et al. WGX50 mitigates doxorubicin-induced cardiotoxicity through inhibition of mitochondrial ROS and ferroptosis. J Transl Med. 2023;21(1):823. https://doi.org/10.1186/s12967-023-04715-1.
36. Wu Z, Huang H, Han Q, et al. SENP7 senses oxidative stress to sustain metabolic fitness and antitumor functions of CD8+ T cells. J Clin Invest. 2022;132(7): e155224. https://doi.org/10.1172/JCI155224.

37. Guo Y, Liu B, Liu Y, et al. Oncogenic chromatin modifier KAT2A activates MCT1 to drive the glycolytic process and tumor progression in renal cell carcinoma. Front Cell Dev Biol. 2021;9: 690796. https://doi.org/10.3389/fcell.2021.690796.
38. Mizukoshi E, Kaneko S. Immune cell therapy for hepatocellular carcinoma. J Hematol Oncol. 2019;12(1):52. https://doi.org/10.1186/s13045-019-0742-5.
39. Dominguez D, Ye C, Geng Z, et al. Exogenous IL-33 restores dendritic cell activation and maturation in established cancer. J Immunol. 2017;198(3):1365–75. https://doi.org/10.4049/jimmunol.1501399.
40. Kustermann M, Klingspor M, Huber-Lang M, Debatin KM, Strauss G. Immunostimulatory functions of adoptively transferred MDSCs in experimental blunt chest trauma. Sci Rep. 2019;9(1):7992. https://doi.org/10.1038/s41598-019-44419-5.
41. Challen GA, Boles NC, Chambers SM, Goodell MA. Distinct hematopoietic stem cell subtypes are differentially regulated by TGF-beta1. Cell Stem Cell. 2010;6(3):265–78. https://doi.org/10.1016/j.stem.2010.02.002.
42. Beerman I, Bhattacharya D, Zandi S, et al. Functionally distinct hematopoietic stem cells modulate hematopoietic lineage potential during aging by a mechanism of clonal expansion. Proc Natl Acad Sci USA. 2010;107(12):5465–70. https://doi.org/10.1073/pnas.1000834107.
43. Liu Y, Van Zant G, Liang Y. Measuring the aging process in stem cells. Methods Mol Biol. 2015;1235:19–32. https://doi.org/10.1007/978-1-4939-1785-3_3.
44. Liu Z, Wu Y, Zhang Y, et al. TIGAR promotes tumorigenesis and protects tumor cells from oxidative and metabolic stresses in gastric cancer. Front Oncol. 2019;9:1258. https://doi.org/10.3389/fonc.2019.01258.
45. Takubo K, Nagamatsu G, Kobayashi CI, et al. Regulation of glycolysis by Pdk functions as a metabolic checkpoint for cell cycle quiescence in hematopoietic stem cells. Cell Stem Cell. 2013;12(1):49–61. https://doi.org/10.1016/j.stem.2012.10.011.
46. Thongon N, Ma F, Santoni A, et al. Hematopoiesis under telomere attrition at the single-cell resolution. Nat Commun. 2021;12(1):6850. https://doi.org/10.1038/s41467-021-27206-7.
47. Netherby CS, Messmer MN, Burkard-Mandel L, et al. The granulocyte progenitor stage is a key target of IRF8-mediated regulation of myeloid-derived suppressor cell production. J Immunol. 2017;198(10):4129–39. https://doi.org/10.4049/jimmunol.1601722.
48. Li X, Liu M, Liu H, Chen J. Tumor metabolic reprogramming in lung cancer progression. Oncol Lett. 2022;24(2):287. https://doi.org/10.3892/ol.2022.13407.
49. Hou G, Lu Z, Yang Z, Jiang J. Prognostic value of metabolic genes in lung adenocarcinoma via integrative analyses. Genomics. 2022;114(4): 110425. https://doi.org/10.1016/j.ygeno.2022.110425.
50. Huang X, Trinh T, Aljoufi A, Broxmeyer HE. Hypoxia signaling pathway in stem cell regulation: good and evil. Curr Stem Cell Rep. 2018;4(2):149–57. https://doi.org/10.1007/s40778-018-0127-7.
51. Mistry JJ, Marlein CR, Moore JA, et al. ROS-mediated PI3K activation drives mitochondrial transfer from stromal cells to hematopoietic stem cells in response to infection. Proc Natl Acad Sci USA. 2019;116(49):24610–9. https://doi.org/10.1073/pnas.1913278116.
52. Folmes CD, Dzeja PP, Nelson TJ, Terzic A. Metabolic plasticity in stem cell homeostasis and differentiation. Cell Stem Cell. 2012;11(5):596–606. https://doi.org/10.1016/j.stem.2012.10.002.
53. Li W, Tanikawa T, Kryczek I, et al. Aerobic glycolysis controls myeloid-derived suppressor cells and tumor immunity via a specific CEBPB isoform in triple-negative breast cancer. Cell Metab. 2018;28(1):87-103.e6. https://doi.org/10.1016/j.cmet.2018.04.022.
54. Uehara I, Kajita M, Tanimura A, et al. 2-Deoxy-d-glucose induces deglycosylation of proinflammatory cytokine receptors and strongly reduces immunological responses in mouse models of inflammation. Pharmacol Res Perspect. 2022;10(2): e00940. https://doi.org/10.1002/prp2.940.
55. Prabhu NB, Vinay CM, Satyamoorthy K, Rai PS. Pharmacogenomics deliberations of 2-deoxy-d-glucose in the treatment of COVID-19 disease: an in silico approach. 3Biotech. 2022;12(11):287. https://doi.org/10.1007/s13205-022-03363-4.
56. Kaira K, Kuji I, Kagamu H. Value of ^{18}F-FDG-PET to predict PD-L1 expression and outcomes of PD-1 inhibition therapy in human cancers. Cancer Imaging. 2021;21(1):11. https://doi.org/10.1186/s40644-021-00381-y.
57. Li B, Yang T, Liu J, et al. Genetically engineered PD-1 displaying nanovesicles for synergistic checkpoint blockades and chemo-metabolic therapy against non-small cell lung cancer. Acta Biomater. 2023;161:184–200. https://doi.org/10.1016/j.actbio.2023.03.002.
58. Papafragkos I, Grigoriou M, Boon L, Kloetgen A, Hatzioannou A, Verginis P. Ablation of NLRP3 inflammasome rewires MDSC function and promotes tumor regression. Front Immunol. 2022;13:889075. https://doi.org/10.3389/fimmu.2022.889075.
59. Wang G, Li J, Bojmar L, et al. Tumour extracellular vesicles and particles induce liver metabolic dysfunction. Nature. 2023;618(7964):374–82. https://doi.org/10.1038/s41586-023-06114-4.

Publisher's Note